

Advanced 3D Micro-Electrodes for On-Chip Zinc-Ion Micro-Batteries

Nibagani Naresh, Yijia Zhu, Jingli Luo, Yujia Fan, Tianlei Wang, Kumar Raju, Michael De Volder, Ivan P. Parkin, and Buddha Deka Boruah*

The development of high-performance planar micro-batteries featuring safer, cost-effective systems is crucial for powering smart devices such as medical implants, micro-robots, micro-sensors, and the Internet of Things (IoT). However, current on-chip micro-batteries suffer from limited energy density within constrained device footprints due to challenges in effectively loading high-capacity active materials onto micro-electrodes. Innovative designs for advanced micro-electrodes are needed for on-chip micro-batteries. This work introduces advanced, highly porous 3D gold (Au) scaffold-based interdigitated electrodes (IDEs) as current collectors, which enable effective loading of active materials (Zn and polyaniline) without compromising overall conductivity and significantly increase active mass loading. These 3D Au scaffold-based micro-batteries (3D P-ZIMB) offer substantially higher energy storage performance ($\approx 135\%$ enhancement) compared to conventional micro-batteries (C-ZIMB) when materials loaded onto flat Au IDEs. Furthermore, the 3D P-ZIMB demonstrates higher areal capacities ($\approx 35 \mu\text{Ah cm}^{-2}$) and areal energy ($\approx 31.05 \mu\text{Wh cm}^{-2}$) than most high-performance on-chip micro-batteries, and it delivers a much higher areal power ($\approx 3584.35 \mu\text{W cm}^{-2}$) than high-performance on-chip micro-supercapacitors. In-depth postmortem investigations reveal that the 3D P-ZIMB avoids issues like material peeling, sluggish electrolyte ion diffusion, and dendrite formation on the anode, while maintaining identical material morphologies and structural characteristics. Therefore, this study presents a smart strategy to enhance the electrochemical performance of planar micro-batteries and advance the field of on-chip micro-battery research.


millimeter-scale computing systems, micro-robots, micro-sensors, and the IoT.^[1,2] For these on-chip micro-electronic devices to function effectively and uninterruptedly, high-energy density and compatible energy storage systems are essential.^[3–5] Planar on-chip micro-batteries are a promising candidate in this regard, as they offer higher energy density than micro-supercapacitors while maintaining competitive power density and cycling stability.^[6–8] Moreover, safety is a critical requirement for micro-batteries, especially in applications such as medical implants.^[9] Li-ion micro-batteries encounter safety issues, potential leakage, and the formation of toxic HF due to reactions involving the electrolyte.^[10] In contrast, zinc (Zn)-ion batteries are emerging as a promising candidate for on-chip micro-batteries due to their intrinsic safety, cost-effectiveness, and environmental friendliness. Zn's high theoretical capacity (820 mAh g^{-1}) and low electrochemical potential (-0.76 V vs SHE) allow it to operate in aqueous-based electrolytes, further reducing costs and fire hazards.^[11,12,13,14] Despite these advantages, challenges remain in preventing hydrogen evolution reactions and dendritic growth of Zn during cycling, which can lead to short circuits. Further, it remains a

1. Introduction

Recent advancements in *System-on-Chip* (SoC) technology have significantly improved devices such as medical implants,

a challenge to effectively load large volumes of cathode materials onto micro-electrodes without compromising overall conductivity and structural integrity.^[15,16] Previously reported on-chip ZIMBs have faced challenges such as low mass-loading, poor ion

N. Naresh, Y. Zhu, J. Luo, Y. Fan, B. D. Boruah
Institute for Materials Discovery
University College London
London WC1E 7JE, UK
E-mail: b.boruah@ucl.ac.uk

 The ORCID identification number(s) for the author(s) of this article can be found under <https://doi.org/10.1002/adfm.202413777>

© 2024 The Author(s). Advanced Functional Materials published by Wiley-VCH GmbH. This is an open access article under the terms of the [Creative Commons Attribution](#) License, which permits use, distribution and reproduction in any medium, provided the original work is properly cited.

DOI: 10.1002/adfm.202413777

T. Wang, I. P. Parkin
Department of Chemistry
University College London
London WC1H 0AJ, UK
K. Raju, M. De Volder
Institute for Manufacturing
Department of Engineering
University of Cambridge
Cambridge CB3 0FS, UK

transport and electrical conductivity, peeling during cycling, and dendrite growth.

To address these challenges, innovative electrode design and material engineering are crucial. Developing advanced micro-electrode designs is essential, and one promising approach is utilizing 3D porous structures for effective electrode material loading.^[17] These structures can offer a high surface area for active material loading, facilitate efficient ion transport, and mitigate issues related to dendritic Zn growth by providing more uniform current distribution. In this context, porous 3D Au scaffold-based IDEs present an advanced and effective strategy for enhancing the performance of on-chip ZIMBs. These IDEs serve as current collectors that enable the effective loading of polyaniline (PANI) as the cathode material, offering hybrid charge storage through capacitive and diffusion-controlled charge storage for improved rate capability. Meanwhile, Zn is used as the anode material to achieve higher capacity, enhancing overall energy storage performance without sacrificing conductivity or morphological integrity. Our findings demonstrate that the 3D P-ZIMBs offer substantially higher areal capacities ($\approx 35 \mu\text{Ah cm}^{-2}$) and energy densities ($\approx 31 \mu\text{Wh cm}^{-2}$) compared to micro-batteries with flat Au IDEs (C-ZIMBs), and higher than previously reported on-chip micro-batteries. Moreover, the 3D P-ZIMBs maintain high areal power densities ($\approx 3584 \mu\text{W cm}^{-2}$), exceeding most high-performance micro-supercapacitors. The 3D P-ZIMBs not only provide superior charge storage performance but also demonstrate dendrite-free operation and maintain the cathode material's morphology, which is crucial for advancements in micro-battery technology. Therefore, the establishment of porous 3D Au scaffold-based IDEs with high-capacity material loading paves the way for the development of high-performance, reliable, and safer energy storage solutions for a wide range of on-chip applications.

2. Results and Discussion

The Au IDEs were patterned onto ceramic substrates with a 200 μm gap and width. The ceramic substrates were selected to reduce leakage current across the Au IDEs. Subsequently, 3D porous Au scaffolds was patterned onto the flat IDEs using dynamic bubble techniques through electrodeposition (detailed in the experimental section).^[18,19] This technique generates gas bubbles at the electrode surface, acting as soft templates to create porous or structured coatings. By controlling bubble formation and detachment, the method enhances material deposition, influencing the morphology and properties of the deposited layer, and achieving controlled porosity through regulated gas evolution. **Figure 1a** illustrates the step-by-step procedure for obtaining the 3D porous Au scaffold on the flat Au IDE device. For charge storage, Zn-based anode was loaded onto the porous Au scaffold, offering high theoretical volumetric energy (5845 mAh cm^{-3} and 820 mAh g^{-1}). PANI was chosen as the cathode to provide a hybrid charge storage performance combining capacitive and diffusion-controlled processes within a limited micro-device footprint.^[20,21] The material loading and the porous Au scaffold structures were optimized through a series of electro-deposition process. It was found that 20 seconds of PANI electro-deposition (see supplementary information) onto the porous Au scaffold yielded optimal charge storage performance. The results of these devices are reported throughout the manuscript (details on the

procedures are available in the experimental section). To better understand the advantages of micro-batteries with porous Au scaffold-based IDEs (3D P-ZIMB), conventional micro-batteries were also fabricated by loading PANI and Zn onto flat Au IDEs under the same experimental conditions for a fair comparison (C-ZIMBs). It is expected that the 3D P-ZIMB electrodes will facilitate rapid electron transportation across electrodes and 3D diffusion of Zn^{2+} ions (**Figure 1b**), improving charge storage capacities over the device footprint. **Figure 1c** shows digital images of the devices. Notably, even with the same PANI deposition time on IDEs, the porous Au scaffold IDEs exhibited higher current compared to flat Au IDEs, indirectly indicating more PANI deposition (**Figure S1**, Supporting Information). However, accurately measuring mass loading is challenging due to the small scale, and thus it was not reported in the study. To gain further insight into the thickness of the micro-electrodes in the micro-batteries, profilometer scanning was performed. **Figure 1d** demonstrates 2D and 3D views with the height profile of 3D P-ZIMB, confirming successful micro-battery fabrication without short circuits. The measured thicknesses of the Zn anode and PANI cathode are 7 and 17 μm , respectively (excluding flat Au IDEs, which are around 4 μm as shown in **Figure S2**, Supporting Information). In contrast, the thicknesses for Zn and PANI deposited onto flat Au IDEs are 6 μm and 11 μm , respectively (**Figure S3**, Supporting Information). It was noted that Zn and PANI deposition was more efficient and prominent on the porous Au scaffold IDEs than on flat Au IDEs. This efficiency is mainly due to the increased surface area, which allows effective deposition on the porous Au scaffold and provides better conductivity without compromising electrode thickness, thereby increasing charge storage performance over the limited device footprint (see further details).

The SEM images at different magnifications in **Figures 2a–c** demonstrate the successful deposition of the porous Au scaffold on flat Au IDEs, achieved without any short-circuit issues under optimal deposition conditions. The highly porous Au scaffold structures were formed due to dynamic bubble generation during electrodeposition, resulting in porous structures. **Figure 2d–f** show SEM images of the 3D P-ZIMB at various magnifications, illustrating the successful loading of Zn for the anode and PANI for the cathode onto the respective porous Au IDEs without disrupting the original Au scaffold. The Zn deposition onto the porous Au maintains the scaffold-like structure (**Figure 2g,h**) but decreases overall porosity due to precise Zn coating, as confirmed by the magnified images of the Zn anode, which display highly dense nanosheet-like morphologies (**Figure 2i**). In contrast, the PANI fully covers the porous Au after 20 s of deposition, although some cracks appear (**Figure 2j**) due to the thicker PANI layer. The magnified images (**Figures 2k,l**) reveal that the deposited PANI retains nanowire-like morphologies with distinct porosities, which is advantageous for effective Zn^{2+} ion interaction on the PANI cathode surface, potentially enhancing charge storage performance. To further understand the morphological characteristics of Zn and PANI when coated on flat Au IDEs, we extended SEM investigations to the C-ZIMB (**Figure S4** (Supporting Information) shows SEM images of Au IDEs at different magnifications). Interestingly, no significant differences in the morphologies of Zn and PANI were observed between 3D P-ZIMB and C-ZIMB, with both maintaining identical densely packed nanosheet-like morphologies for Zn and

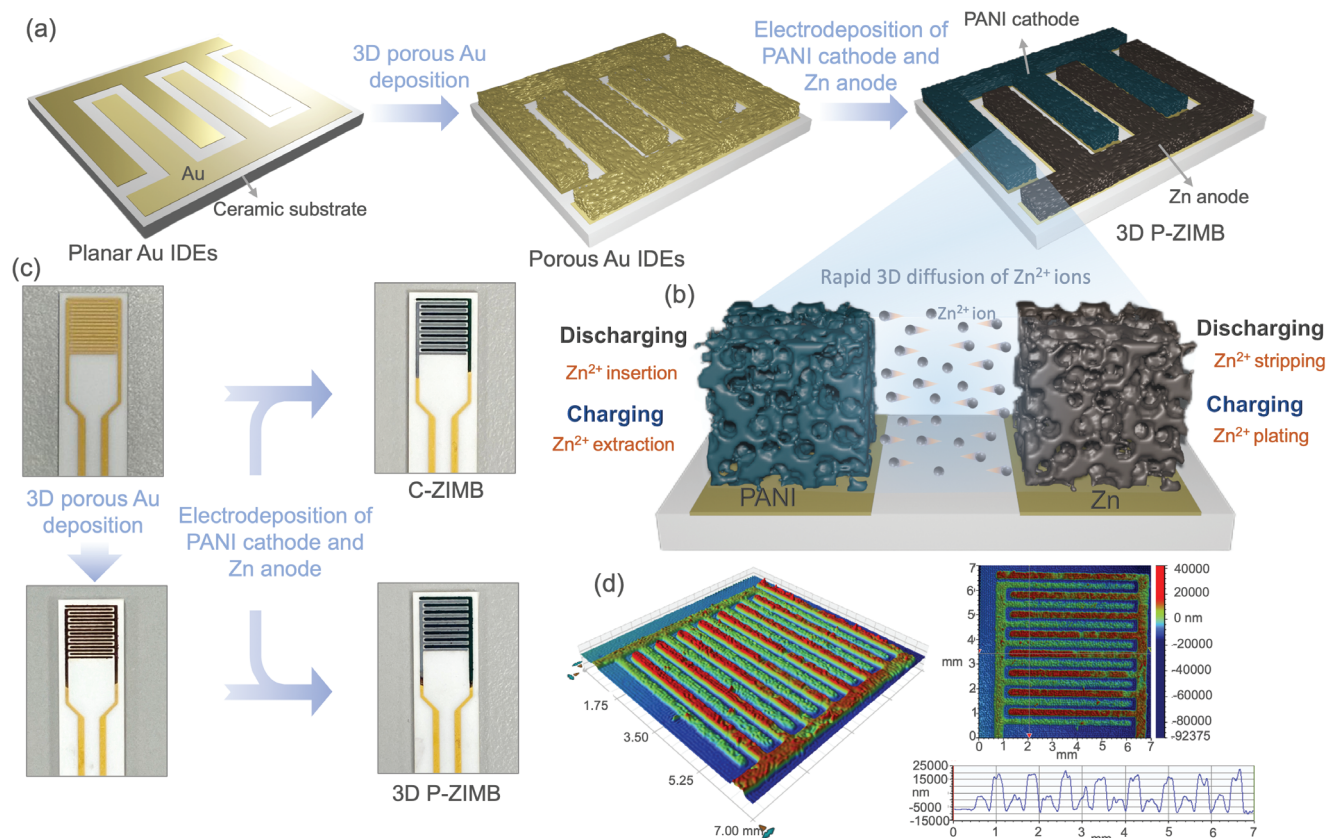


Figure 1. a) Schematic illustration of the steps in the fabrication of 3D P-ZIMBs, including the design of the porous Au scaffold on flat Au IDEs, followed by the sequential deposition of the PANI cathode and Zn anode onto the respective micro-electrodes. b) Schematic demonstration of the 3D in-plane diffusion of Zn^{2+} ions during discharging, where Zn^{2+} ions strip from the Zn anode and insert into the PANI cathode, and during charging, where Zn^{2+} ions extract from the PANI cathode and plate onto the Zn anode. c) Digital images of the obtained electrodes: flat Au IDEs, 3D porous Au scaffold IDEs, as well as the devices C-ZIMB and 3D P-ZIMB. d) 2D and 3D profilometer images of 3D P-ZIMB, with the lower image showing height profiles of the electrodes, measured to be 21 and 7 μm , respectively, including the flat Au IDEs thickness, which is around 4 μm .

nanowire-like morphologies for PANI while preserving porosities (refer to Figure S5, Supporting Information).

Moreover, we extended additional structural characterization of the electrodeposited Zn and PANI, as shown in Figure 2m,n. For performing XRD analysis, the electrodeposited Zn and PANI samples were deposited on titanium (Ti) foil using the same experimental conditions, as the IDEs are too small for XRD measurements. The XRD pattern of electrodeposited Zn (Figure 2m) shows distinct characteristic peaks at around $2\theta = 36.53^\circ$, 39.26° , 43.38° , and 54.56° , corresponding to the diffraction planes of (002), (100), (101), and (102), respectively, and peaks can be well indexed to hexagonal zinc.^[22] The XRD pattern of electrodeposited PANI displays distinct broad peaks at approximately 15.42° , 20.45° , and 25.57° , corresponding to the (011), (020), and (200) reflections, respectively. This indicates crystalline regions within an amorphous matrix.^[23] Additionally, the Raman spectrum of PANI shows characteristic peaks at around 1192 cm^{-1} , 1345 cm^{-1} , 1492 cm^{-1} , and 1617 cm^{-1} , corresponding to C–H bending deformation in the benzenoid ring, C–N⁺ stretching, C=N stretching vibration, and C=C stretching of quinoid, respectively.^[24]

Next, the charge storage performance of the C-ZIMBs and 3D P-ZIMBs was evaluated using a gel electrolyte consisting of 3 M

$\text{Zn}(\text{CF}_3\text{SO}_3)_2$ in guar gum (see the experimental section for detailed composition of the gel electrolyte). The electrochemical responses were measured by immersing the micro-batteries in the gel electrolyte within a cuvette (Figure S6, Supporting Information, a digital image). Figure S7 (Supporting Information) shows the CV curves of C-ZIMBs and 3D P-ZIMBs at various scan rates ($0.2\text{--}0.6\text{ mV s}^{-1}$) over a voltage window of $0.5\text{--}1.5\text{ V}$. Distinct pairs of redox peaks were observed, corresponding to the two-step intercalation and de-intercalation of Zn^{2+} ions into the PANI matrix during discharging and charging.^[25,26] Additionally, simultaneous proton (H^+) doping and de-doping may occur, contributing to capacitive-based charge storage. Notably, 3D P-ZIMBs exhibited similar CV patterns to C-ZIMBs but with significantly higher areal currents. Comparative CVs at scan rates of 0.4 mV s^{-1} (Figure 3a) and 0.6 mV s^{-1} (Figure 3b) clearly demonstrate the enhanced area enclosed by the CV curves, indicating improved charge storage performance in 3D P-ZIMBs. To gain a deeper understanding of the charge storage contributions, b -values for specific oxidation and reduction peaks were calculated using the relation $i_p = av^b$, where a and b are constants.^[27] The b -value ranges from 0.5 to 1, with values close to 0.5 indicating diffusion-controlled performance and values near 1.0 suggesting capacitive-controlled charge storage. Figure 3c shows

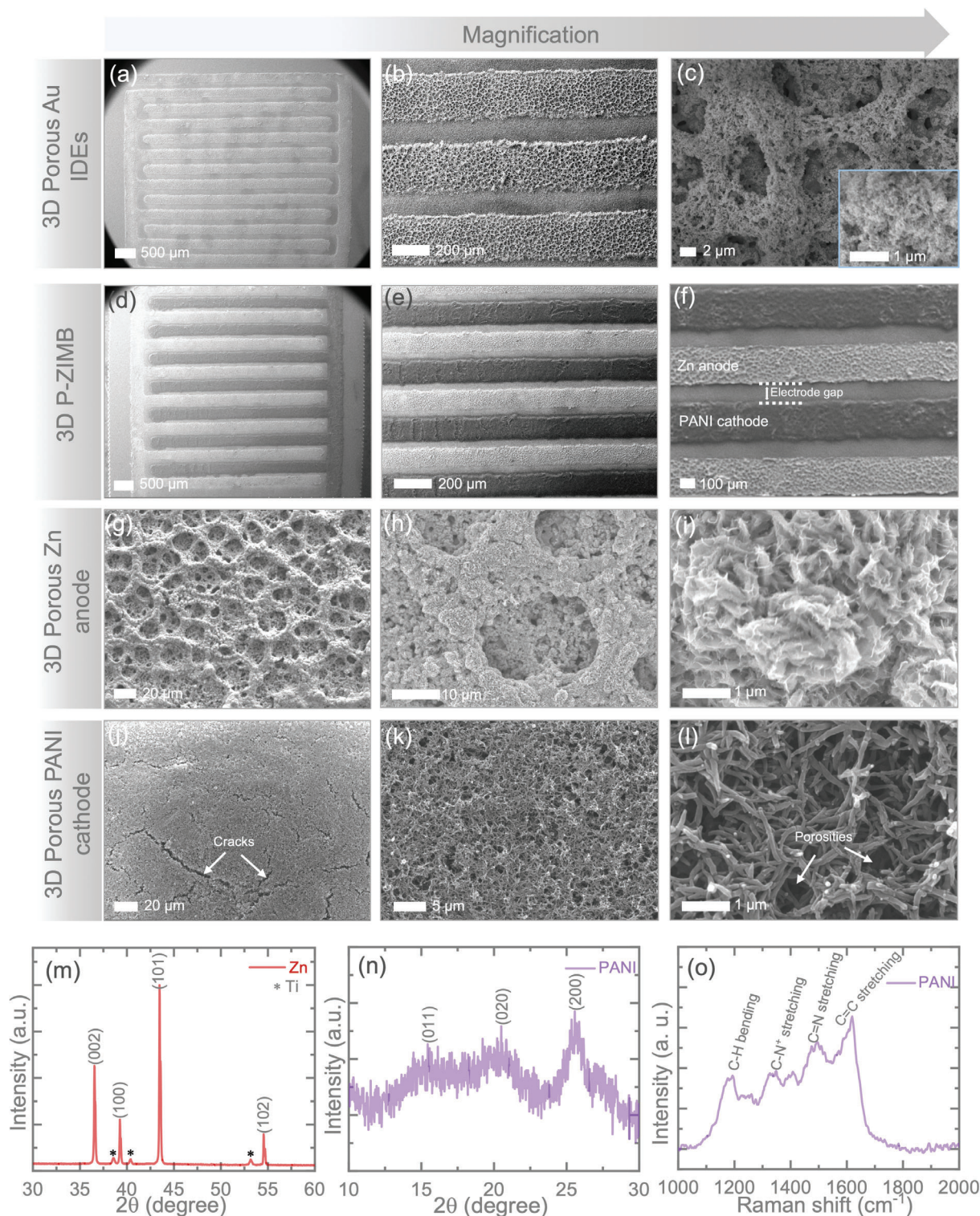


Figure 2. a–c) SEM images of 3D porous Au scaffold IDEs at different magnifications, demonstrating the successful and uniform distribution of porosity in the Au scaffold on flat Au IDEs. d,e) SEM images of the 3D P-ZIMB at different magnifications, showing successful loading of electrode materials onto the porous Au scaffold IDEs. g–i) Further magnified images of the 3D porous Zn anode, demonstrating efficient loading of Zn onto the porous Au scaffold without destroying its structure, although the overall porosity is reduced due to the Zn coating. j–l) Magnified images of PANI-coated porous Au scaffold IDEs, showing full coverage with PANI, which increase the mass loading of PANI and thus enhance the overall areal capacity. The further magnified images reveal that the PANI has a nanowire-like morphology with distinct porosities, potentially increasing effective interaction with the electrolyte and interfaces. m,n) XRD patterns of electrodeposited Zn and PANI. For XRD analysis, Zn and PANI were electrodeposited onto Ti substrates under the same conditions used for the micro-batteries. o) Raman spectrum of electrodeposited PANI.

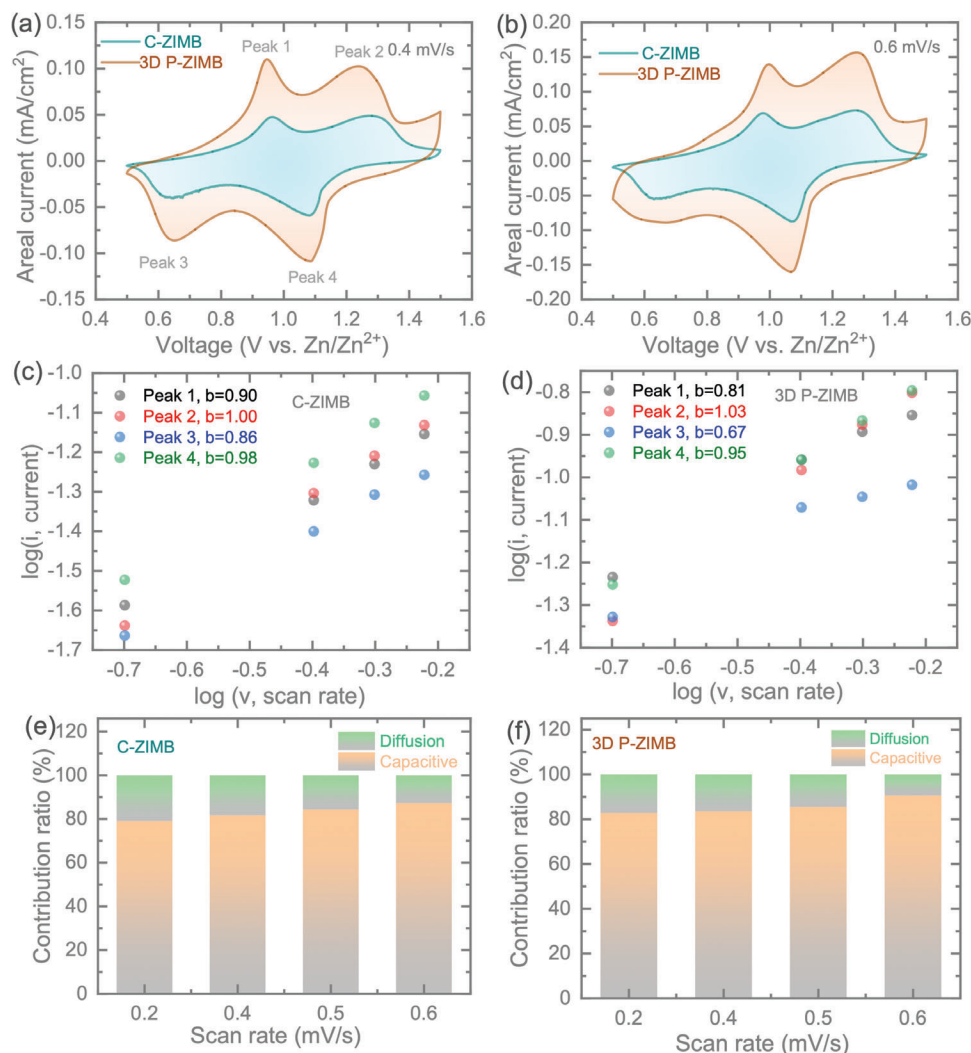


Figure 3. CVs of C-ZIMB and 3D P-ZIMB at different scan rates of a) 0.4 mV s^{-1} and b) 0.6 mV s^{-1} over the voltage window of $0.5\text{--}1.5 \text{ V}$. Calculation of b -values for the cathodic and anodic peaks for c) C-ZIMB and d) 3D P-ZIMB, where b -values approaching 1 for most peaks in both micro-batteries indicate that the overall charge storage is dominated by capacitive control, which can lead to high-rate capability of the micro-batteries. e, f) Calculation of capacitive-controlled and diffusion-controlled contributions at different scan rates, showing that more than 80% of charge storage contributions come from capacitive-controlled processes.

the b -value calculations for the cathodic and anodic peaks of C-ZIMB, which are ≈ 0.90 (peak 1), 1.00 (peak 2), 0.86 (peak 3), and 0.98 (peak 4). These values, mostly approaching 1.0, indicate capacitive-dominated charge storage contributions. Similarly, for 3D P-ZIMB, the b -values are 0.81 , 1.03 , 0.67 , and 0.95 , respectively. Furthermore, the charge storage process can be quantified into capacitive-controlled ($k_1 v$) and diffusion-controlled ($k_2 v^{0.5}$) components based on the current at a fixed voltage relation, $i(V) = k_1 v + k_2 v^{0.5} \Rightarrow i(V)/v^{0.5} = k_1 v^{0.5} + k_2$.^[28] The capacitive-controlled contributions were 79.10% and 82.87% at 0.2 mV s^{-1} for C-ZIMB and 3D P-ZIMB, respectively, slightly increasing to 87.24% and 90.56% for C-ZIMB and 3D P-ZIMB at a scan rate of 0.6 mV s^{-1} . Figure 3e,f presents the contribution plots relative to scan rates for C-ZIMB and 3D P-ZIMB. This analysis further confirms that the charge storage contribution of our micro-batteries is dominated by a capacitive-controlled charge storage mechanism. The introduction of porous Au scaffold IDEs as cur-

rent collectors further enhances the capacitive-controlled charge storage mechanism, which is advantageous for high-rate battery operation (see further details).

Furthermore, we performed galvanostatic charge–discharge (GCD) testing of the C-ZIMB and 3D P-ZIMB at different areal currents ranging from $50 \mu\text{A cm}^{-2}$ to $1000 \mu\text{A cm}^{-2}$. Figure 4a,b shows the respective GCD curves of C-ZIMB and 3D P-ZIMB at areal currents of 50 , 100 , 200 , 300 , 400 , 500 , and $1000 \mu\text{A cm}^{-2}$ over a voltage range of $0.5\text{--}1.5 \text{ V}$. Consistent with the CV responses, the 3D P-ZIMB demonstrates significantly improved areal capacities compared to the C-ZIMB. Specifically, the areal capacities increase from 15 to $35 \mu\text{Ah cm}^{-2}$ and from 6.8 to $16 \mu\text{Ah cm}^{-2}$ at areal currents of $50 \mu\text{A cm}^{-2}$ and $1000 \mu\text{A cm}^{-2}$, respectively, in the 3D P-ZIMB compared to the C-ZIMB, as shown in Figure 4c,d. Even at higher areal currents, the 3D P-ZIMB maintains significant improvements in areal capacity ($\approx 135\%$), which highlights the advantages of micro-batteries with a porous

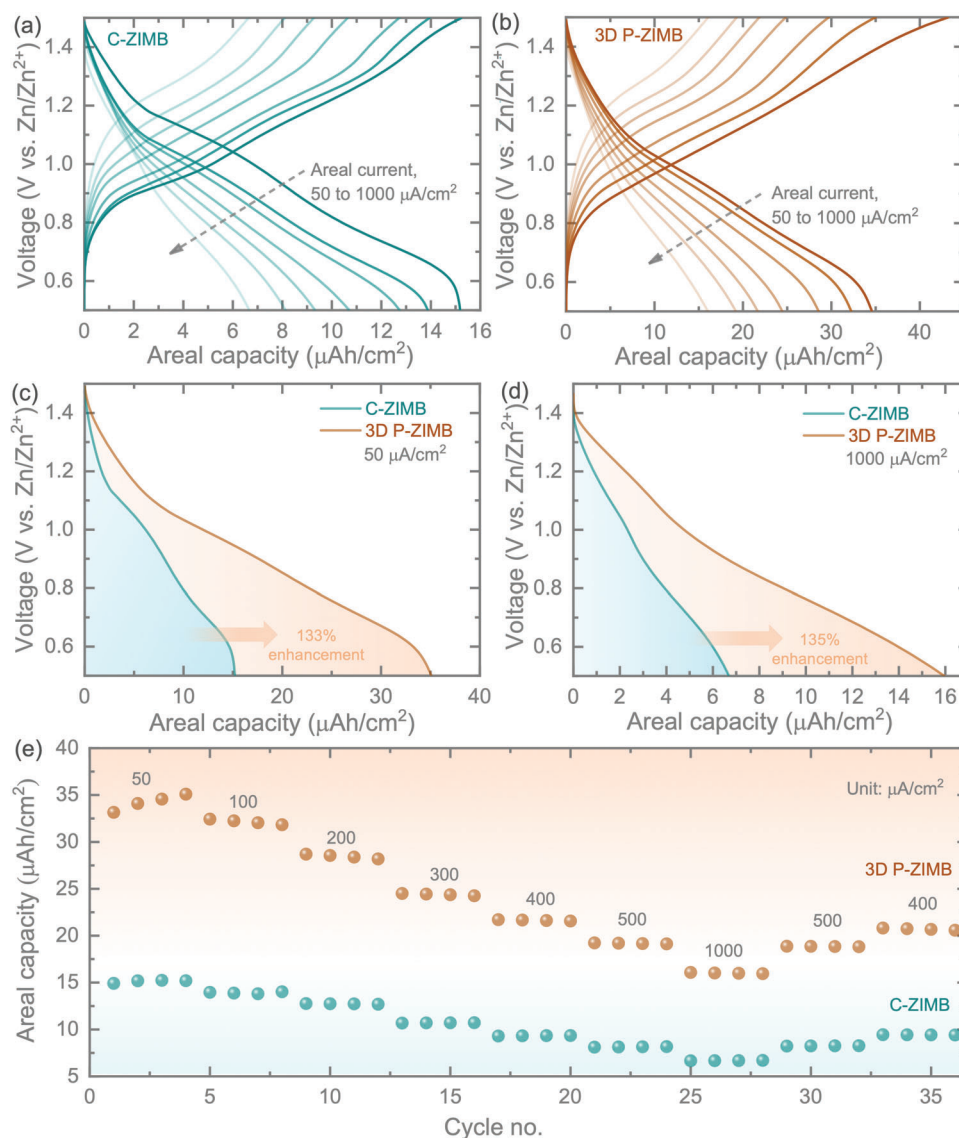


Figure 4. GCDs of a) C-ZIMB and b) 3D P-ZIMB at different areal currents ranging from $50 \mu\text{A cm}^{-2}$ to $1000 \mu\text{A cm}^{-2}$ over a voltage window of $0.5\text{--}1.5 \text{ V}$. c,d) Comparative GCDs of the C-ZIMB and 3D P-ZIMB show a significant increase in areal capacities from 15 to $35 \mu\text{Ah cm}^{-2}$ and 6.8 to $16 \mu\text{Ah cm}^{-2}$ at areal currents of $50 \mu\text{A cm}^{-2}$ and $1000 \mu\text{A cm}^{-2}$, respectively, in 3D P-ZIMB compared to C-ZIMB. e) Rate test of the C-ZIMB and 3D P-ZIMB at different areal currents, increasing from $50 \mu\text{A cm}^{-2}$ to $1000 \mu\text{A cm}^{-2}$ and then back to $400 \mu\text{A cm}^{-2}$.

3D Au scaffold. The rate test performance of the C-ZIMB and 3D P-ZIMB, shown in Figure 4e, further confirms the significant enhancement in areal capacities at each areal current and efficient reversibility. The 3D P-ZIMB offers reasonably efficient charge storage capacities of nearly 19.30 and $16.00 \mu\text{Ah cm}^{-2}$ at higher areal currents of 500 and $1000 \mu\text{A cm}^{-2}$, respectively, while the C-ZIMB only achieves 8.20 and $6.8 \mu\text{Ah cm}^{-2}$. These results demonstrate that the 3D P-ZIMB not only provides higher areal capacities at lower rates but also maintains reasonably good charge storage performance at high rates, attributed to the capacitive-controlled dominant charge storage mechanism of the device. However, the initial increase in areal capacity of the 3D P-ZIMB may be attributed to the activation of the 3D porous PANI micro-electrodes as the 3D porous mi-

croelectrodes have more PANI coating than planar Au IDEs, which contributes to the activation process. Capacitive-controlled charge storage offers both improve charge storage performance and rate capability. The areal capacities of our 3D P-ZIMBs are significantly larger than those of reported micro-batteries, including planar types: Carbon//Polymer (half-cell $31 \mu\text{Ah cm}^{-2}$, full cell $10.6 \mu\text{Ah cm}^{-2}$),^[29] Ni-NiO//Zn,^[30] Ni//Bi,^[31] thin-film micro-batteries: $\text{LiCoO}_2/\text{Li}_4\text{Mn}_5\text{O}_{12}$ ^[32] and sandwich-type thin film solid-state batteries: $\text{V}_2\text{O}_5/\text{Li}_x\text{V}_2\text{O}_5$ ($6 \mu\text{Ah cm}^{-2}$),^[33] $\text{LiMn}_2\text{O}_4/\text{V}_2\text{O}_5$ ($18 \mu\text{Ah cm}^{-2}$),^[34] and $\text{V}_2\text{O}_5/\text{Li}_x\text{Mn}_2\text{O}_4$,^[35] respectively. Additionally, we calculated the volumetric capacities of both C-ZIMB and 3D P-ZIMB (see Figure S8, Supporting Information). For example, at an areal current of $50 \mu\text{A cm}^{-2}$, the volumetric capacities of 3D P-ZIMB and C-ZIMB are 20.77 and

13.96 mAh cm⁻³, respectively. These results further highlight the advantages and effectiveness of our porous 3D electrodes in enhancing charge storage compared to the planar IDEs. Furthermore, it is demonstrated that our 3D P-ZIMB can efficiently power commercial sensors. For instance, two 3D P-ZIMBs connected in series can easily power an indoor-outdoor thermometer with a hygrometer clock (as shown in Figure S9, Supporting Information), showcasing the potential to expand the application capabilities of on-chip micro-batteries. To further understand the charge transfer kinetics of the micro-batteries, we extended the EIS testing, with results provided in the Supporting Information. The Nyquist plot (Figure S10, Supporting Information) shows that the 3D P-ZIMB has demonstrates charge-transfer resistance of 5.5 Ω compared to the C-ZIMB's 260 Ω. Additionally, the equivalent series resistance is lower for the 3D P-ZIMB, with efficient diffusion kinetics at high frequencies (refer Figure S10, Supporting Information). Therefore, our porous Au IDEs not only offer higher charge storage performance within a limited device footprint but also maintain lower charge transfer resistance, without compromising conductivity. Moreover, we extended our analysis to estimate the relative change in the diffusion constants of Zn²⁺ ions (refer to Figure S11, Supporting Information). In this analysis, the real impedance is related to the diffusion coefficient as follows: $Z' = (R_L + R_D) + \sigma\omega^{-0.5}$ and $D_{Zn^{2+}} = \frac{R^2 T^2}{2A^2 \eta^4 F^4 C^2 \sigma^2} = \frac{K}{\sigma^2}$; where ($R_L + R_D$) represents the total resistance (including solution and charge transfer), Z' is the real impedance component from the Nyquist plot, $D_{Zn^{2+}}$ is the diffusion coefficient of Zn²⁺ ion (cm² s⁻¹), σ is the Warburg coefficient, ω is the angular frequency, n is the number of electrons transferred per electrolyte per monomer unit of PANI, T is the cell testing temperature in Kelvin (298.13 K), A is the active electrode area (cm²), R is the molar gas constant (8.314 J K⁻¹ mol⁻¹), F is Faraday's constant (96 485.3383 C mol⁻¹), and C is the Zn²⁺ ion molar concentration used in the electrolyte.^[36] Since the electrode area and electrolyte concentrations are the same for both C-ZIMB and 3D P-ZIMB, the value of K (where $K = \frac{R^2 T^2}{2A^2 \eta^4 F^4 C^2 \sigma^2}$) can be considered identical for both micro-batteries. This allows us to compare the relative change in the Zn²⁺ ion diffusion coefficients. As shown in Figure S11 (Supporting Information), the slope of the $Z' \text{ Vs } \omega^{-0.5}$ graph is related to σ , where a lower σ indicates a higher $D_{Zn^{2+}}$, and vice versa. Therefore, the lower slope observed in the 3D P-ZIMB micro-batteries indicates a higher Zn²⁺ ion diffusion coefficient compared to the C-ZIMB.

Next, the extended GCDs of the C-ZIMB and 3D P-ZIMB for 100 cycles, shown in Figure 5a, reveal stable performance over cycling. The measured capacity retentions are 108.56% (the capacity retention exceeding 100% is primarily attributed to the increasing capacities with cycling due to the material activation process) and 94.25% for C-ZIMB and 3D P-ZIMB, respectively, with coulombic efficiencies of 100% (Figure S12, Supporting Information), respectively. Hence, 3D P-ZIMB not only maintains stable charge storage performance over cycling (100 cycles) but also retains improved capacities. To gain a deeper understanding of the cycling stability of our 3D P-ZIMB, we evaluated its long-term performance over 200 cycles (see Figure S13, Supporting Information). The 3D P-ZIMB retained ≈50% of its capacity after 200 cycles. The observed capacity fading after 100 cycles may be attributed to the cracking of the PANI micro-cathodes

(see further details). Additionally, we conducted a self-discharge measurement of the 3D P-ZIMB (refer to Figure S14, Supporting Information), and even after 25 h, our 3D P-ZIMB maintained a voltage of 0.95 V. For further insight into the stability of the micro-electrodes, we conducted *ex-situ* SEM and Raman investigations of the cycled devices, with the digital images of the cycled devices shown in Figure 5b. Figure 5c displays the post-mortem SEM images of the cycled C-ZIMB, including low magnification images (i, ii) to confirm the absence of short circuits, and higher magnification images. The magnified SEM images of the PANI cathode (iii, iv) reveal cracks throughout the micro-electrodes but maintain nanowire-like PANI morphologies. The increasing cracks after cycling could be due to the presence of small cracks between the nanowire-like PANI framework in the PANI electrodes before cycling, which could propagate further through stress generation across the micro-electrodes under repetitive cycling. On the other hand, significant dendrite growth on the edges of the Zn anodes was recorded, as shown in the magnified images (vi and vii). It is not surprising that the edges of electrodes could generate intense electric field distributions due to the in-plane diffusion of Zn²⁺ ions, leading to the formation of dendrites. Similarly, Figure 5d shows the SEM images of the cycled 3D P-ZIMB, where the PANI cathode displays more prominent cracks (ii–iv) due to the high mass loading of PANI, which leads to more stress generation during cycling, while maintaining the original nanowire-like PANI morphologies. On the other hand, no noticeable dendrite growth was observed on the edges of the Zn anode in 3D P-ZIMB (v), unlike the anode of C-ZIMB, but the electrodes maintained identical morphologies and porosities. Zn flakes growth was observed in some places on the micro-electrodes due to the preferred growth direction of metallic Zn during the repetitive Zn²⁺ plating/stripping process. Although cracking of PANI cathode was observed in our 3D P-ZIMBs, there was no observation of material peeling off from the porous Au IDEs, which is an additional advantage. Our advanced porous Au micro-electrodes not only allow higher loading of the cathode materials, in this case, PANI, but also hold the materials onto the electrode geometries to minimize peeling off. The cracking of the micro-electrode materials could be improved to further enhance the cycling stability of the micro-batteries through advanced coating of materials with zincophilic characteristics onto the micro-electrodes, which could mechanically suppress crack propagation and equally suppress dendrite growth, as observed in the Zn anode in C-ZIMB. Furthermore, the *ex situ* Raman investigation of cycled PANI (shown in Figure S15, Supporting Information) maintained identical material characteristics, with the characteristic Raman peaks attributed to the pristine PANI, i.e., before cycling. Hence, PANI could be a potential cathode material for Zn-ion micro-batteries, demonstrating reversible capacitive-controlled charge storage performance for high-rate capability while maintaining morphologies and structural characteristics.

Furthermore, we calculated the areal energy and areal power density for the C-ZIMB and 3D P-ZIMB as shown in Figure S16 (Supporting Information), which clearly demonstrates notable enhancements in the areal energy density of the 3D P-ZIMB without compromising power performance. This indicates that our 3D P-ZIMB can deliver significantly higher energies with similar power compared to the C-ZIMB. The calculated areal energies (at areal powers) for the 3D P-ZIMB are ≈31.05 μWh cm⁻²

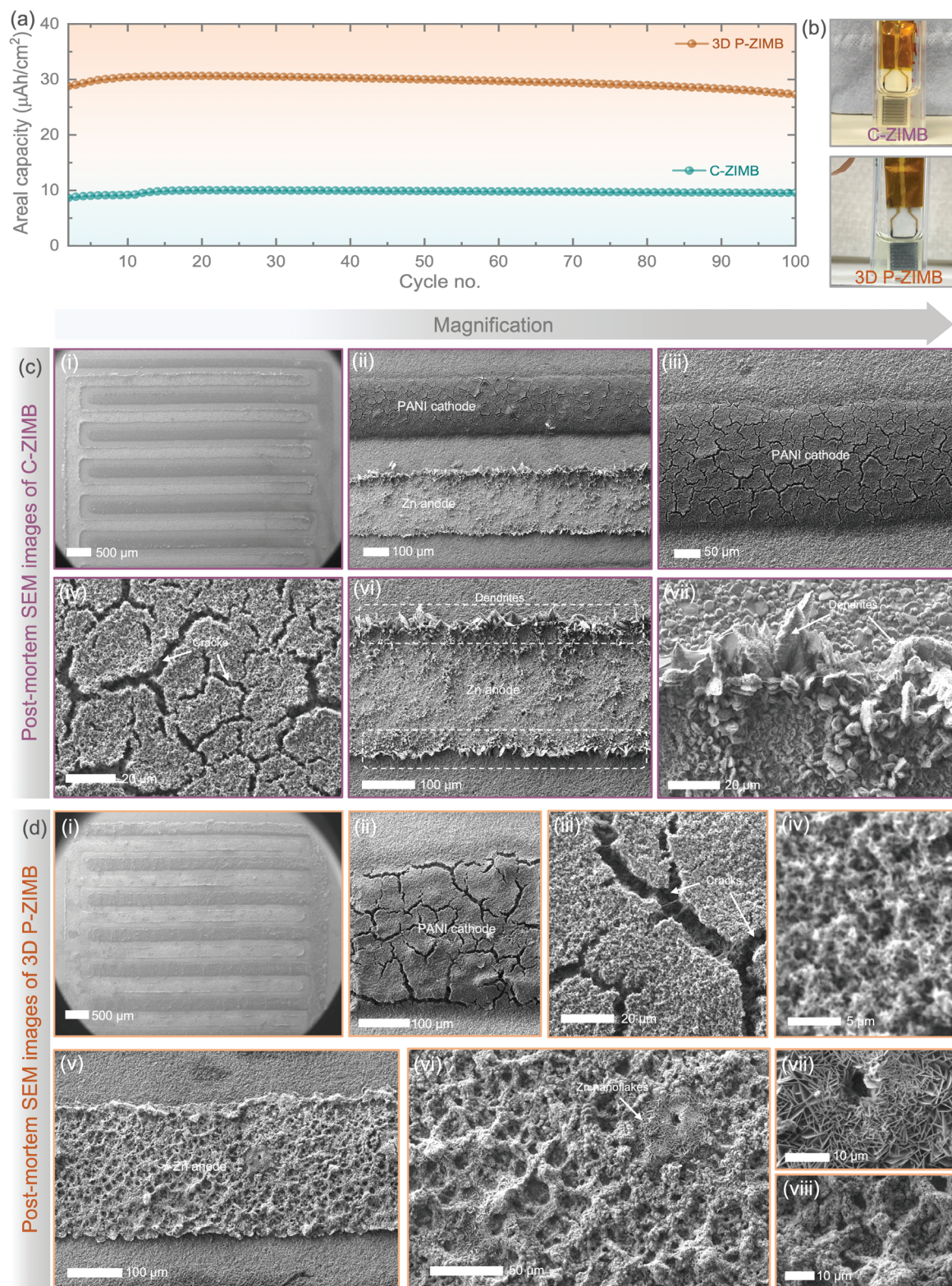


Figure 5. a) Extended long-term cycling tests of the C-ZIMB and 3D P-ZIMB for 100 cycles, with observed capacity retentions of $\approx 108.56\%$ and $\approx 94.25\%$ for C-ZIMB and 3D P-ZIMB, respectively. b) Digital images of the cycled micro-batteries: C-ZIMB and 3D P-ZIMB. c) Postmortem SEM images of a cycled C-ZIMB at different magnifications. High magnification images clearly illustrate the cracking of the PANI cathode after cycling, but also demonstrate the growth of Zn dendritic-like morphologies on the edges of the Zn anodes. d) SEM images of cycled 3D P-ZIMB: larger cracking of the PANI cathodes is displayed, however, the nanowire-like PANI morphologies are maintained even after cycling. The porous 3D Zn anode did not display noticeable dendrite growth, maintaining an identical 3D porous structure, although some Zn flakes growth occurred due to the preferred growth direction of metallic Zn.

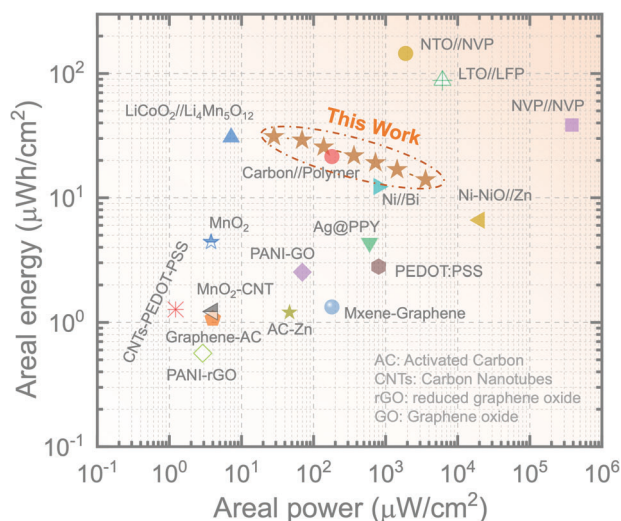


Figure 6. Ragone plot comparing the areal energies and areal powers of our 3D P-ZIMB with various published micro-batteries: Carbon//Polymer,^[29] Ni-NiO//Zn,^[30] Ni//Bi,^[31] thin-film batteries: LiCoO₂//Li₄Mn₅O₁₂,^[32] and micro-supercapacitors: Mxene-Graphene,^[37] PANI-rGO,^[38] MnO₂-CNT,^[39] CNTs-PEDOT-PSS,^[40] MnO₂,^[41] Ag@PPY,^[42] polyaniline/graphite oxide,^[43] PEDOT:PSS,^[44] AC-Zn,^[45] Graphene-AC,^[46] LTO//LFP,^[47] NVP//NVP,^[48] NTO//NVP.^[49]

($\approx 28 \mu\text{W cm}^{-2}$) and $\approx 14 \mu\text{Wh cm}^{-2}$ ($\approx 3584 \mu\text{W cm}^{-2}$), which are $\approx 14 \mu\text{Wh cm}^{-2}$ ($\approx 39 \mu\text{W cm}^{-2}$) and $\approx 6 \mu\text{Wh cm}^{-2}$ ($\approx 3542 \mu\text{W cm}^{-2}$) for the C-ZIMB, respectively. The areal energies of our 3D P-ZIMB are higher than most reported on-chip energy storage devices shown in **Figure 6** (Ragone plot), for instance, including micro-batteries: Carbon//Polymer,^[29] Ni-NiO//Zn,^[30] Ni//Bi,^[31] and thin-film micro-batteries: LiCoO₂//Li₄Mn₅O₁₂.^[32] Our 3D P-ZIMB not only delivers higher areal energy density but also offers higher areal powers, which are comparable to or even higher than high-performance micro-supercapacitors: Mxene-Graphene,^[37] PANI-rGO,^[38] MnO₂-CNT,^[39] CNTs-PEDOT-PSS,^[40] MnO₂,^[41] Ag@PPY,^[42] polyaniline/graphite oxide,^[43] PEDOT:PSS,^[44] AC-Zn,^[45] and Graphene-AC,^[46] respectively. Hence, our findings further confirm the advantages of our advanced micro-electrodes in delivering high-energy storage performance within a limited device footprint. The performance of our 3D P-ZIMB is lower than that of previously reported Li-ion and Na-ion micro-batteries, which were made using a mask-assisted vacuum filtering technique with a larger device area ($\approx 1.68 \text{ cm}^2$) and wider IDE finger widths (around 1 mm), compared to our 3D P-ZIMB (device area including electrode gap is 0.36 cm^2 , with IDE widths and gaps of 200 μm).^[47–49] This difference in performance is expected, given the higher material loading on the larger 1 mm IDE fingers and the higher voltage of Li and Na-based systems compared to the safer Zn-based systems. Nevertheless, it is crucial to minimize the IDE gaps, device area, and width to achieve effective integration with system-on-a-chip technology and enhance the charge storage performance of micro-batteries within a limited device area. The fabrication of a series of porous microelectrodes on a wafer scale is feasible using our approach. The processing method described in this work is both efficient and rapid, offering precise control over porosity with minimal challenges. However, PANI deposited on the 3D porous Au electrodes tends to develop

cracks, which propagate and enlarge during repeated charge and discharge cycles, leading to capacity fading. Therefore, there is potential to explore methods to suppress capacity fading, such as introducing SEI layers to enhance long-term cycling stability. Additionally, these 3D electrodes address common issues in micro-batteries, such as electrode flaking, sluggish ion diffusion, and dendrite formation on the Zn anode. Consequently, this work paves the way for developing more efficient, high-performing, and safer on-chip micro-batteries, which are essential for the advancement of smart system-on-chip devices.

3. Conclusions

This study showcases a significant advancement in the design and performance of planar Zn-ion micro-batteries using highly porous 3D gold scaffold-based interdigitated electrodes. By efficiently loading high-capacity active materials—polyaniline (PANI) for the cathode and zinc (Zn) for achieving higher capacities—onto these advanced micro-electrodes, the developed 3D P-ZIMB micro-batteries exhibit markedly improved energy storage performance ($31 \mu\text{Wh cm}^{-2}$), higher areal capacities ($35 \mu\text{Ah cm}^{-2}$), and great power output ($3584 \mu\text{W cm}^{-2}$). This innovative design also addresses common issues in micro-batteries such as electrode flaking, sluggish ion diffusion, and dendrite formation while maintaining the structural integrity of the active materials. Consequently, this work paves the way for the development of more efficient, high-performing, and safer on-chip micro-batteries, which are crucial for the continued progress of smart system-on-chip devices.

Supporting Information

Supporting Information is available from the Wiley Online Library or from the author.

Acknowledgements

B.D.B. acknowledges support from the EPSRC research grant EP/Y008103/1. B.D.B. and M.D.V. acknowledge support from the EPSRC research grant EP/Y008332/1.

Conflict of Interest

The authors declare no conflict of interest.

Data Availability Statement

The data that support the findings of this study are available from the corresponding author upon reasonable request.

Keywords

3D porous gold scaffold, high-performance, on-chip micro-batteries, Polyaniline, zinc

Received: July 30, 2024
Revised: August 27, 2024
Published online:

- [1] Q. Xia, F. Zan, Q. Zhang, W. Liu, Q. Li, Y. He, J. Hua, J. Liu, J. Xu, J. Wang, C. Wu, H. Xia, *Adv. Mater.* **2023**, 35, 2200538.
- [2] A. Toor, A. Wen, F. Maksimovic, A. M. Gaikwad, K. S. J. Pister, A. C. Arias, *Nano Energy* **2021**, 82, 105666.
- [3] Z. Qu, M. Zhu, Y. Yin, Y. Huang, H. Tang, J. Ge, Y. Li, D. D. Karnaushenko, D. Karnaushenko, O. G. Schmidt, *Adv. Energy Mater.* **2022**, 12, 2200714.
- [4] Y. Liu, S. Zheng, J. Ma, X. Wang, L. Zhang, P. Das, K. Wang, Z. S. Wu, *Adv. Energy Mater.* **2022**, 12, 2200341.
- [5] S. Zheng, X. Shi, P. Das, Z. S. Wu, X. Bao, *Adv. Mater.* **2019**, 31, 1900583.
- [6] P. Li, M. Liao, J. Li, L. Ye, X. Cheng, B. Wang, H. Peng, *Small Struct.* **2022**, 3, 2200058.
- [7] C. Dai, L. Hu, X. Jin, Y. Wang, R. Wang, Y. Xiao, X. Li, X. Zhang, L. Song, Y. Han, H. Cheng, Y. Zhao, Z. Zhang, F. Liu, L. Jiang, L. Qu, *Sci. Adv.* **2022**, 8, eabo6688.
- [8] X. Jin, L. Song, C. Dai, Y. Xiao, Y. Han, X. Li, Y. Wang, J. Zhang, Y. Zhao, Z. Zhang, N. Chen, L. Jiang, L. Qu, *Adv. Mater.* **2022**, 34, 2109450.
- [9] K. Jiang, X. Wen, Y. Deng, Z. Zhou, Q. Weng, *SusMat.* **2022**, 2, 368.
- [10] J. Ma, R. Quhe, W. Zhang, Y. Yan, H. Tang, Z. Qu, Y. Cheng, O. G. Schmidt, M. Zhu, *Small.* **2023**, 19, 2300230.
- [11] M. Song, H. Tan, D. Chao, H. J. Fan, *Adv. Funct. Mater.* **2018**, 28, 1802564.
- [12] B. Tang, L. Shan, S. Liang, J. Zhou, *Energy Environ. Sci.* **2019**, 12, 3288.
- [13] R. Wang, S. Xin, D. Chao, Z. Liu, J. Wan, P. Xiong, Q. Luo, K. Hua, J. Hao, C. Zhang, *Adv. Funct. Mater.* **2022**, 32, 2207751.
- [14] R. Wang, Q. Ma, L. Zhang, Z. Liu, J. Wan, J. Mao, H. Li, S. Zhang, J. Hao, L. Zhang, C. Zhang, *Adv. Energy Mater.* **2023**, 13, 2302543.
- [15] L. E. Blanc, D. Kundu, L. F. Nazar, *Joule.* **2020**, 4, 771.
- [16] X. Hu, J. Borowiec, Y. Zhu, X. Liu, R. Wu, A. M. Ganose, I. P. Parkin, B. D. Boruah, *Small.* **2024**, 20, 2306827.
- [17] J. Ni, A. Dai, Y. Yuan, L. Li, J. Lu, *Matter.* **2020**, 2, 1366.
- [18] S. Cherevko, C. H. Chung, *Electrochim. Commun.* **2011**, 13, 16.
- [19] S. Cherevko, C. H. Chung, *Electrochim. Acta.* **2010**, 55, 6383.
- [20] F. Wan, L. Zhang, X. Wang, S. Bi, Z. Niu, J. Chen, *Adv. Funct. Mater.* **2018**, 28, 1804975.
- [21] R. Han, Y. Pan, C. Yin, C. Du, Y. Xiang, Y. Wang, H. Zhu, *J. Colloid Interface Sci.* **2023**, 650, 322.
- [22] P. Zhang, Y. Li, G. Wang, F. Wang, S. Yang, F. Zhu, X. Zhuang, O. G. Schmidt, X. Feng, *Adv. Mater.* **2019**, 31, 1806005.
- [23] M. Mitra, C. Kulsi, K. Chatterjee, K. Kargupta, S. Ganguly, D. Banerjee, S. Goswami, *RSC Adv.* **2015**, 5, 31039.
- [24] Y. Zhang, J. Liu, Y. Zhang, J. Liu, Y. Duan, *RSC Adv.* **2017**, 7, 54031.
- [25] H. Yan, X. Mu, Y. Song, Z. Qin, D. Guo, X. Sun, X. X. Liu, *Chem. Commun.* **2022**, 58, 1693.
- [26] H. Y. Shi, Y. J. Ye, K. Liu, Y. Song, X. Sun, *Angew. Chemie – Int. Ed.* **2018**, 57, 16359.
- [27] B. D. Boruah, B. Wen, M. De Volder, *ACS Nano.* **2021**, 15, 16616.
- [28] B. Deka Boruah, A. Mathieson, S. K. Park, X. Zhang, B. Wen, L. Tan, A. Boies, M. De Volder, *Adv. Energy Mater.* **2021**, 11, 2100115.
- [29] H. S. Min, B. Y. Park, L. Taherabadi, C. Wang, Y. Yeh, R. Zaouk, M. J. Madou, B. Dunn, *J. Power Sources.* **2008**, 178, 795.
- [30] Y. Zeng, Y. Meng, Z. Lai, X. Zhang, M. Yu, P. Fang, M. Wu, Y. Tong, X. Lu, *Adv. Mater.* **2017**, 29, 1702698.
- [31] L. He, T. Hong, X. Hong, X. Liao, Y. Chen, W. Zhang, H. Liu, W. Luo, L. Mai, *Energy Technol.* **2019**, 7, 1900144.
- [32] M. Kotobuki, Y. Suzuki, H. Munakata, K. Kanamura, Y. Sato, K. Yamamoto, T. Yoshida, *Electrochim. Acta.* **2011**, 56, 1023.
- [33] M. Baba, N. Kumagai, H. Kobayashi, O. Nakano, K. Nishidate, *Electrochim. Solid-State Lett.* **1999**, 2, 320.
- [34] M. Baba, N. Kumagai, N. Fujita, K. Ohta, K. Nishidate, S. Komaba, H. Groult, D. Devilliers, B. Kaplan, *J. Power Sources.* **2001**, 97–98, 798.
- [35] J. B. Bates, N. J. Dudney, D. C. Lubben, G. R. Gruzalski, B. S. Kwak, X. Yu, R. A. Zuh, *J. Power Sources.* **1995**, 54, 58.
- [36] R. Nandan, N. Takamori, K. Higashimine, R. Badam, N. Matsumi, *J. Mater. Chem.* **2022**, 10, 15960.
- [37] Y. Yue, N. Liu, S. Wang, W. Liu, C. Luo, H. Zhang, F. Cheng, J. Rao, X. Hu, J. Su, Y. Gao, *ACS. Nano.* **2018**, 12, 4224.
- [38] S. Park, H. Lee, Y. Kim, P. S. Lee, *NPG Asia Mater.* **2018**, 10, 959.
- [39] J. Yun, H. Lee, C. Song, Y. Ra, J. Woo, J. Ho, D. Sik, K. Keum, M. Su, S. Woo, Y. Hui, J. Wook, *Chem. Eng. J.* **2020**, 387, 124076.
- [40] H. Xiao, Z. S. Wu, F. Zhou, S. Zheng, D. Sui, Y. Chen, X. Bao, *Energy Storage Mater.* **2018**, 13, 233.
- [41] B. Asbani, B. Bounor, K. Robert, C. Douard, L. Athouël, *J. Electrochem. Soc.* **2020**, 167, 100551.
- [42] L. Liu, Q. Lu, S. Yang, J. Guo, Q. Tian, W. Yao, Z. Guo, V. A. L. Roy, W. Wu, *Adv. Mater. Technol.* **2018**, 3, 1700206.
- [43] H. Wei, J. Zhu, S. Wu, S. Wei, Z. Guo, *Polymer.* **2013**, 54, 1820.
- [44] Y. Fan, T. Wang, R. Asrosa, B. Li, N. Naresh, X. Liu, S. Guan, R. Li, M. Wang, I. P. Parkin, B. Deka, *Chem. Eng. J.* **2024**, 488, 150672.
- [45] Y. Fan, X. Liu, N. Naresh, Y. Zhu, I. Pinnock, T. Wang, M. Wang, I. P. Parkin, B. D. Boruah, *J. Mater. Chem.* **2024**, 11710.
- [46] H. Chen, S. Chen, Y. Zhang, H. Ren, X. Hu, Y. Bai, *ACS Appl. Mater. Interfaces.* **2020**, 12, 56319.
- [47] S. Zheng, Z. Wu, F. Zhou, X. Wang, J. Ma, C. Liu, *Nano Energy.* **2018**, 51, 613.
- [48] X. Wang, H. Huang, F. Zhou, P. Das, P. Wen, *Nano Energy.* **2021**, 82, 105688.
- [49] S. Zheng, H. Huang, Y. Dong, S. Wang, F. Zhou, J. Qin, C. Sun, Y. Yu, Z. Wu, X. Bao, *Energy Environ. Sci.* **2020**, 13, 821.